

Cite this: *Biomater. Sci.*, 2024, **12**, 2599

# Tissue-specific gelatin bioink as a rheology modifier for high printability and adjustable tissue properties†

Hohyeon Han,<sup>‡a</sup> Minji Kim,<sup>‡c</sup> Uijung Yong,<sup>e</sup> Yeonggwon Jo,<sup>a</sup> Yoo-mi Choi,<sup>d</sup> Hye Jin Kim,<sup>b</sup> Dong Gyu Hwang,<sup>d</sup> Dayoon Kang<sup>‡c,d</sup> and Jinah Jang<sup>‡b,c,d,f</sup>

Decellularized extracellular matrix (dECM) has emerged as an exceptional biomaterial that effectively recapitulates the native tissue microenvironment for enhanced regenerative potential. Although various dECM bioinks derived from different tissues have shown promising results, challenges persist in achieving high-resolution printing of flexible tissue constructs because of the inherent limitations of dECM's weak mechanical properties and poor printability. Attempts to enhance mechanical rigidity through chemical modifications, photoinitiators, and nanomaterial reinforcement have often compromised the bioactivity of dECM and mismatched the desired mechanical properties of target tissues. In response, this study proposes a novel method involving a tissue-specific rheological modifier, gelatinized dECM. This modifier autonomously enhances bioink modulus pre-printing, ensuring immediate and precise shape formation upon extrusion. The hybrid bioink with GeldECM undergoes a triple crosslinking system—physical entanglement for pre-printing, visible light photocrosslinking during printing for increased efficiency, and thermal crosslinking post-printing during tissue culture. A meticulous gelatinization process preserves the dECM protein components, and optimal hybrid ratios modify the mechanical properties, tailoring them to specific tissues. The application of this sequential multiple crosslinking designs successfully yielded soft yet resilient tissue constructs capable of withstanding vigorous agitation with high shape fidelity. This innovative method, founded on mechanical modulation by GeldECM, holds promise for the fabrication of flexible tissues with high resilience.

Received 27th December 2023,  
Accepted 17th March 2024

DOI: 10.1039/d3bm02111d

rsc.li/biomaterials-science

## 1. Introduction

Decellularized extracellular matrix (dECM) has emerged as a tissue-specific biomaterial recapitulating the microenvironment of native tissue. Compared to conventional single-type extracellular matrix (ECM) materials, such as collagen and laminin, dECM facilitates cell specification and tissue morphogenesis because of its composition with a diverse bio-

chemical milieu.<sup>1,2</sup> Recent studies have focused on dECM bioinks derived from various tissues ever since they were formulated into hydrogels.<sup>3,4</sup> In addition to highlighting their remarkable regenerative potential across a variety of target tissues *in vitro*,<sup>5,6</sup> the application of dECM bioinks and tissue fabricated with them has shown promising feasibility for its eventual clinical use.<sup>1,7</sup> However, dECM's principal thermal crosslinking mechanism is considerably restricted by the heat transport rate within the gel environment, resulting in inadequate structural stability of the printed constructs with unique geometries (*e.g.*, tubular, curved, spherical).<sup>8</sup> These limitations pose challenges in printing flexible tissue constructs with high resolution; to date, tissue engineering of hollow organs with dECM bioinks mostly relies on polymer scaffolds to ensure tissue geometry and mechanical stability.<sup>9,10</sup>

Alternatively, exogenous additions and modifications of dECM have been tried in various ways to improve their mechanical rigidity. For example, exogenous additions include chemical crosslinkers,<sup>11–14</sup> ionically crosslinkable polymers,<sup>15,16</sup> and reinforcing nanomaterials,<sup>17</sup> whereas chemical modifications typically involve methacrylation.<sup>18–21</sup>

<sup>a</sup>School of Interdisciplinary Bioscience and Bioengineering, Pohang University of Science and Technology (POSTECH), South Korea

<sup>b</sup>Department of Convergence IT Engineering, Pohang University of Science and Technology (POSTECH), South Korea. E-mail: jinahjang@postech.ac.kr

<sup>c</sup>Department of Mechanical Engineering, Pohang University of Science and Technology (POSTECH), South Korea

<sup>d</sup>Center for 3D Organ Printing and Stem Cells, Pohang University of Science and Technology (POSTECH), South Korea

<sup>e</sup>Future IT Innovation Laboratory (i-Lab), Pohang University of Science and Technology (POSTECH), South Korea

<sup>f</sup>Institute of Convergence Science, Yonsei University, South Korea

† Electronic supplementary information (ESI) available. See DOI: <https://doi.org/10.1039/d3bm02111d>

‡ These authors contributed equally to this work.



Unfortunately, they have critical limitations. Chemical modification methods are often detrimental to the inherent bioactivity of pristine dECM because they affect the physical composition of dECM, undermining the original purpose of using dECM bioinks.<sup>22</sup> Furthermore, it is difficult to control the kinetics of the ionic crosslinking, and ionically crosslinked hydrogels tend to swell and dissolve in the aqueous physiological environment.<sup>23,24</sup> Integrating nanomaterials increase the stiffness and brittleness of the bioink,<sup>25</sup> failing to match the soft yet tough properties of the native soft tissues.<sup>26,27</sup>

Our recent method enhanced the printability of dECM using a biocompatible visible light photoinitiator system.<sup>28</sup> However, as with other photocrosslinking methods, it did not improve the properties of the printing ink itself but rather allowed faster and tighter crosslinking of the printed ink and stiffened the hydrogel matrix. In this study, we developed a rheological modifier derived from dECM that can be tailored to specific tissues. This modifier demonstrates the distinctive ability to autonomously enhance the modulus of the bioink in the pre-printing step, facilitating the immediate and precise formation of the desired shape, following the extrusion of the bioink.

Specifically, we incorporated gelatinized dECM (GeldECM) as a mechanical modifier to dECM and aimed to fabricate a triple crosslinking system for the hybrid bioink (Fig. 1). We expected to employ (i) physical entanglement of the GeldECM portion to enhance printability for pre-printing, (ii) visible light photocrosslinking of the whole hybrid bioink during the printing process to boost crosslinking efficiency, and (iii) thermal crosslinking of the dECM portion after printing to culture the bioprinted tissues. We established a gelatinization process that does not deplete the protein components in dECM; additionally, we determined the best hybridization ratio to modify the mechanical properties of the target tissue.

Consequently, we successfully printed cm-scale, tough, and resilient tissue constructs that can withstand vigorous agitation.

We chose small intestine submucosa (SIS) dECM to demonstrate our idea as a promising technique for tissue printing of hollow soft organs. In the future, this sequential multiple crosslinking design based on the mechanical modulatory effect of the GeldECM portion will be useful in fabricating other flexible tissues requiring high resilience.

## 2. Materials and methods

### 2.1. Materials

#### 2.1.1. dECM

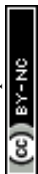
**2.1.1.1. Decellularization of the porcine small intestine.** Porcine small intestine tissue was obtained from the slaughterhouse. The decellularization process was conducted according to a previously reported protocol, in which the only modification involved the transition from colon to small intestine tissue.<sup>29</sup>

**2.1.1.2. Biochemical analysis of SIS dECM.** As described previously, residual DNA, glycosaminoglycans (GAGs), and collagen in both native and decellularized SIS tissues were quantified to validate the efficacy of the decellularization process.<sup>30</sup> The obtained results were compared to normalized relative values.

**2.1.1.3. Proteomic analysis.** Proteomic analysis of SIS dECM and GeldECM was conducted using an ultra-performance liquid chromatography Q-exactive high-resolution mass spectrometer (Q-exactive UHMR hybrid quadrupole-orbitrap; Thermo Fischer Scientific, USA). First, the samples were prepared by in-solution protein digestion into peptides. After lyophilization, the samples were desalted using a C18 micro spin-



Fig. 1 Triple crosslinking strategy using GeldECM as a rheological modifier of dECM.



column. The purified peptide samples were reconstituted in 0.1% formic acid and subsequently injected into the LC-MS/MS system. Mass spectra were automatically analyzed using Proteome Discoverer (version 2.5; Thermo Fischer Scientific, USA). Protein identification was performed by searching the MS/MS data obtained from the peptides against the UniProt database, specifying *Sus scrofa* as the species for both SIS dECM and SIS GeldECM.

**2.1.1.4. Preparation of SIS dECM bioinks.** The lyophilized SIS dECM was digested for 7–10 days using a solution of 0.5 M acetic acid (Merck Millipore, USA) containing pepsin (Sigma-Aldrich, USA). The digested hydrogel was filtered through a 100  $\mu\text{m}$  cell strainer (SPL Life Sciences, Korea) and stored at 4  $^{\circ}\text{C}$ . Before the experiments, the dECM hydrogel was neutralized with 10 N sodium hydroxide solution (NaOH; Biosaesang, Korea) while being maintained on ice and then stored at 4  $^{\circ}\text{C}$ .

**2.1.2. Photoinitiator.** To formulate photocrosslinkable bioinks, a set of visible light-responsive photo-redox catalysts, comprising tris (2,2-bipyridyl) dichlororuthenium(II) hexahydrate (Ru; Sigma-Aldrich, USA) combined with sodium persulfate (SPS; Sigma-Aldrich, USA), was employed.<sup>31</sup> To produce light-activated dERS, GeldERS, and MeTTi-dERS, Ru/SPS was mixed with dECM and GeldECM at concentrations of  $1 \times 10^{-3}$  M/ $10 \times 10^{-3}$  as previously described.<sup>21</sup> The composition and abbreviations of the dECM-based hydrogel systems are summarized in Fig. 2 and Table 1.

**2.1.3. Preparation of SIS GeldECM and transmittance examinations.** The neutralized SIS dECM hydrogels were subjected to denaturation by placing them in a water bath at 60  $^{\circ}\text{C}$  for 3, 12, 24, 72, and 120 h for denaturation.<sup>32</sup> After gelatiniza-

tion, the GeldECMs were stored at 4  $^{\circ}\text{C}$ . To assess the degree of gelatinization, the transmittance spectra of SIS dECM and GeldECM hydrogel were measured using a multimode microplate reader (Varioskan LUX; Thermo Fischer Scientific, USA). Fifty microliters of each hydrogel sample were placed in a 96-well plate. The absorbance spectra were measured in the wavelength range of 300–800  $\text{cm}^{-1}$  at a wavenumber resolution of 1  $\text{cm}^{-1}$ . Subsequently, the transmittance was calculated using the equation below:

$$\text{Transmittance (\%)} = 10^{2-\text{Absorbance}}$$

**2.1.4. Preparation of hybrid bioinks.** A combination of SIS dECM hydrogel, SIS GeldECM hydrogel, and Ru/SPS was formulated into hybrid bioinks and MeTTi-dERS. Before mixing, the GeldECM hydrogel was put in a 37  $^{\circ}\text{C}$  water bath for less than 10 min to achieve a sol-state suitable for mixing with the dECM hydrogel. The sol-state GeldECM was then blended at a specific ratio with the dECM hydrogel, followed by the introduction of Ru/SPS. To obtain a homogeneous bioink without GeldECM entanglements, the hybrid hydrogel was filtered through a 100  $\mu\text{m}$  cell strainer (SPL Life Sciences, Korea).

## 2.2. Molecular characterization of GeldECM

**2.2.1. Amino acid analysis.** The amino acid content was quantified using an amino acid autoanalyzer (LA8080; Hitachi, Japan). Briefly, the samples were hydrolyzed and separated using an ion exchange column. Following post-column derivatization with ninhydrin, the samples were analyzed at two wavelengths: 570 and 440 nm.

**2.2.2. FTIR.** To investigate the structural differences between dECM and GeldECM, a Fourier-transform infrared (FTIR) spectrometer (VERTEX 70; Bruker, USA) was used for chemical analysis. The analysis was conducted in the spectral range of 4000–500  $\text{cm}^{-1}$  with 64 scans at a wavenumber resolution of 4  $\text{cm}^{-1}$ .

**2.2.3. SDS-PAGE.** For a qualitative analysis of collagen within the dECM and GeldECM hydrogels, sodium dodecyl sulfate (SDS)-polyacrylamide gel electrophoresis (PAGE) was employed, using 4–20% precast protein gel (Bio-Rad Laboratories, USA). The hydrogels were lyophilized and reconstituted in RIPA to obtain a 1% concentration. Subsequently, 10  $\mu\text{L}$  of hydrogel solutions, representing an equivalent amount of protein, along with a standard (spectra multicolor high range protein ladder; Thermo Fischer Scientific, USA), were loaded into the gel wells and subjected to electrophoresis. The protein concentration of each sample was determined using the BCA protein assay kit (Thermo Fischer Scientific, USA).

## 2.3. Mechanical properties of GeldERS

**2.3.1. Compressive test.** Compressive test was conducted using a MicroTester G2 (CellScale, Canada). Cylindrical GeldERS samples were shaped using an acrylic mold with both a diameter and height of 5 mm. To initiate the crosslinking of GeldERS, light exposure occurred for 2 min, and the samples were subsequently shielded from light before experiments to

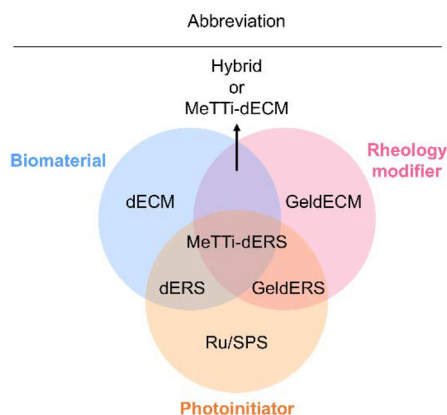


Fig. 2 Venn diagram of the composition of bioinks.

Table 1 Abbreviations and full names of hydrogel systems in this study

Abbreviation	Full name
dECM	Decellularized extracellular matrix
dERS	dECM + Ru/SPS
GeldECM	Gelatinized dECM
MeTTi-dECM	Mechanically tuned tissue-specific dECM
MeTTi-dERS	MeTTi-dECM + Ru/SPS



prevent further photocrosslinking. The samples were placed on testing anvils and compressed using a microbeam (diameter: 0.5588 mm, typical force resolution: 34.52  $\mu\text{N}$ ) with a 6  $\times$  6 mm stainless steel plate glued to the end. The test employed a displacement-controlled mode, with the compression set at 4% strain per min.

**2.3.2. Tensile test.** A tensile test was also conducted using the same equipment employed for the compressive test. The specimens were prepared in a cuboid shape (length: 6.5 mm, width: 3 mm, height: 1.5 mm). Both ends of the samples were stuck to the tension forks on the equipment, and the samples were stretched at a constant velocity of 2 mm  $\text{min}^{-1}$  until rupture.

## 2.4. Assessment of MeTTi-dECM

**2.4.1. Rheological analysis.** The rheological properties of the bioinks were assessed using a rheometer (Discovery HR-2; TA Instruments, USA). To perform each analysis, a 20 mm disposable aluminum parallel plate was used, and a 100  $\mu\text{L}$  sample was placed between the parallel plates with a gap of 300  $\mu\text{m}$  between them.

**2.4.1.1. Time sweep.** A time sweep analysis was conducted to measure the complex modulus of the bioinks. To evaluate the photocrosslinking properties of dERS, GeldERS, and MeTTi-dERS, visible light irradiation started at 180 s with an intensity of 10  $\text{mW cm}^{-2}$  and was continued until the experiments finished. The angular frequency was applied in the range of 0.1 to 100  $\text{rad s}^{-1}$  under a 2% strain for all experiments. Oscillation of dECM, dERS, GelDECM, and MeTTi-dERS occurred at 4  $^{\circ}\text{C}$ , whereas GeldERS oscillated at 37  $^{\circ}\text{C}$ .

**2.4.1.2. Temperature ramp.** A temperature ramp analysis was performed to identify the temperature-dependent crosslinking properties of dERS, GeldERS, and MeTTi-dERS. The temperature was initially held at 4  $^{\circ}\text{C}$  for 180 s, followed by a ramp from 4 to 37  $^{\circ}\text{C}$  at a rate of 5  $^{\circ}\text{C min}^{-1}$ . The temperature was then maintained at 37  $^{\circ}\text{C}$  for 40 min to induce thermal crosslinking in dERS and MeTTi-dERS. Visible light was exposed for 180 s at an intensity of 10  $\text{mW cm}^{-2}$  to photocrosslink MeTTi-dERS. To investigate the physical crosslinking properties of GeldERS, the oscillation temperature was ramped from 37  $^{\circ}\text{C}$  to 4  $^{\circ}\text{C}$  at a rate of 2  $^{\circ}\text{C min}^{-1}$ . A constant angular frequency of 10  $\text{rad s}^{-1}$  and a 2% strain were applied for all experiments.

**2.4.1.3. Flow sweep.** A steady-state flow sweep analysis was conducted to measure the viscosities of MeTTi-dERS at shear rates ranging from 0.1 to 1000  $\text{s}^{-1}$ , at temperatures of 4, 20, and 37  $^{\circ}\text{C}$ .

**2.4.2. Printability test.** A 3D printer based on microextrusion (3DXPrinter; T&R Biofab, Korea) was used, incorporating commercially available nozzles of varying diameters: 24 G (Musashi Engineering Inc., Japan), 21 G (NanoNC, Korea), and 19 G (NanoNC, Korea). The prepared dERS and MeTTi-dERS bioinks were loaded into a syringe equipped with a plunger and placed in a dispenser pre-cooled to 4  $^{\circ}\text{C}$ . Furthermore, LED was used to enable the simultaneous crosslinking of the printed structures.

**2.4.2.1. Strand formation test.** To evaluate the gelation status of the ink and the uniformity of the strands, extrusion was continued through a 19 G nozzle at 5 kPa until the strands tore off.

**2.4.2.2. Shape fidelity analysis.** To assess the expansion of bioinks upon extrusion from the nozzle, which results from the release of shear stress, the expansion degree of the filaments was calculated using the equation:  $\alpha = D/d$ . To demonstrate the ability to print complex structures, the aspect ratio was calculated as the ratio between the actual height and diameter ( $H/D$ ). To estimate the collapse of structures in the vertical direction caused by the effect of gravity, the sinking degree was calculated using the equation:  $\gamma = H/H_0$ .<sup>33</sup> To evaluate the diffusion of strands in the horizontal direction, the ratio between the theoretical diameter and the actual diameter was calculated using the equation:  $\delta = D/D_0$ .

**2.4.3. Evaluation of tissue resilience.** To assess the resilience of the printed tissues, mechanical agitation was applied at a rate of 300 RPM for 15 s using an orbital shaker. This agitation was conducted before the incubation of the tissues.

## 2.5. Assessment of cell viability and maturity

Caco-2 cells (Korea Cell Line Bank, Korea) were encapsulated in dERS and MeTTi-dERS at a density of  $5 \times 10^6$  cells per mL. Cells were cultured using Dulbecco's modified Eagle's medium high glucose (Hyclone, USA) with media replacement occurring every 2 days.

**2.5.1. Cell viability assay.** The viability of cells printed with different nozzle diameters was evaluated using a LIVE/DEAD Viability/Cytotoxicity Kit (Thermo Fischer Scientific, USA) according to the manufacturer's instructions. Fluorescence images of live and dead cells were acquired using a fluorescent confocal laser scanning microscope (Nikon Ti Eclipse, Nikon Instruments, Japan). Quantification of cell viability was conducted using the ImageJ software.

**2.5.2. Cryosectioning.** Thick tissues were processed into cryosections, followed by immunofluorescence staining and imaging. The cultured tissues were fixed with 4% paraformaldehyde (ChemBio, USA) and subsequently dehydrated with 15 and 30% sucrose solutions at 4  $^{\circ}\text{C}$ . Following the removal of sucrose, the tissues were embedded in an optimal cutting temperature (OCT) compound in a cryomold, frozen at  $-80^{\circ}\text{C}$  until solidified and cut into 50  $\mu\text{m}$ -thick sections.

**2.5.3. Immunofluorescence analysis.** The cryosectioned samples were used for mucin staining in printed tissues. The samples were fixed in 4% paraformaldehyde and washed with PBS containing 0.05% Tween-20 (Georgiachem, USA) (PBS-T) thrice for 5 min each time; they were washed with PBS containing 0.1% Triton X-100 for 10 min. Subsequently, the samples were washed again with PBS-T thrice for 5 min each. Next, 10% BSA was used for blocking for 1 h. The primary antibody, mucin 5AC (Abcam, USA) was diluted to obtain a 1:100 ratio in PBS-T and incubated overnight at 4  $^{\circ}\text{C}$ . After three washes with PBS-T, the secondary antibody, Alexa Fluor 488 goat anti-rabbit antibody (Thermo Fischer Scientific, USA), was diluted to obtain a 1:200 ratio with 1% BSA in PBS-T and incubated



for 2 h at room temperature. The samples were washed thrice with PBS-T. Finally, VECTASHIELD mounting medium with DAPI (Vector Laboratories, USA) was applied to stain the nucleus and mount the samples. Immunofluorescence imaging was conducted using a spinning disc confocal microscope (Eclipse Ti2-E, Nikon Instruments, Japan).

For staining the junctional protein markers, the tissues were fixed with 4% paraformaldehyde (ChemBio, USA), washed with DPBS for 5 min, and permeabilized with 0.1% Triton X-100 (Biosesang, Korea) in PBS for 1 h at 25 °C. The samples were washed twice using Hank's balanced salt solution (HBSS, Sigma-Aldrich, USA) with 0.05% Tween-20 and DPBS, each for 5 min. Subsequently, they were treated with 5% normal goat serum (NGS; Invitrogen Life Technologies, USA) for blocking for 1 h and washed with PBS for 5 min each. The primary antibody, E-CAD (Cell Signaling, USA), was then prepared as a 1:100 dilution in 1% BSA and incubated at 4 °C overnight. Next, the secondary antibody, Alexa Fluor 594 goat anti-rabbit antibody (Thermo Fischer Scientific, USA), was diluted to obtain a 1:200 ratio and incubated at 4 °C overnight. The samples were washed twice with HBSS and 0.05% Tween-20 and with DPBS for 5 min. Finally, the antifade mounting medium, VECTASHIELD (Vector Laboratories, USA), was used for nucleus staining and sample mounting. Immunofluorescence imaging was performed using a fluorescent confocal laser scanning microscope (Nikon Ti Eclipse; Nikon Instruments, Japan).

## 2.6. Statistical analysis

Quantitative results were analyzed with GraphPad Prism 10.1.0 (GraphPad Software, USA), and the data are presented as mean  $\pm$  standard deviation (S.D.) or standard error of the mean (S.E. M.) as specifically indicated. Student's *t*-tests were employed to determine the differences between the experimental groups. Statistically significant differences are represented as follows: \**p* < 0.05, \*\**p* < 0.01, \*\*\**p* < 0.001, and \*\*\*\**p* < 0.0001.

# 3. Results and discussion

## 3.1. Preparation of SIS dECM

**3.1.1. Decellularization of SIS tissue.** We decellularized porcine SIS tissue and obtained SIS-specific ECM (Fig. 3A). Decellularization removed the porcine DNA from the native tissue, while retaining GAGs and collagen contents (Fig. 3B). The porcine DNA content was effectively reduced to  $23.04 \pm 1.56$  ng mg<sup>-1</sup> (native SIS:  $280.45 \pm 3.4$  ng mg<sup>-1</sup>). GAGs and collagen contents were relatively enriched as the cellular components were removed compared to the native tissue ( $222.69 \pm 9.98\%$  and  $119.0 \pm 38.91\%$ , respectively).

**3.1.2. Characterization of SIS dECM.** Proteomic analysis revealed a significant amount of collagen types 1 and 5, followed by substantial amounts of fibrillin 1, collagen 4, and collagen 3 in the top 5 most abundant proteins (Fig. 3C). We conducted gene ontology analysis based on proteomic results and classified them according to different functions, such as cellu-

lar components, biological processes, and molecular functions (Fig. 3D).

We evaluated the crosslinking characteristics of SIS dECM and dERS at different concentrations. As previously mentioned, we aimed to develop a triple crosslinking platform where the mechanical properties of dECM bioink can be tuned as desired with the aid of GeldECM. For the designed triple crosslinking strategy to function well, it is important to determine the conditions in which the base hydrogel system, dECM in this study, and the modifier, *i.e.*, GeldECM, have the highest crosslinking efficiency. Increasing the temperature from 4 °C to 37 °C enabled stable thermal crosslinking of the SIS dECMs at all concentrations (Fig. 3E). We assessed the complex modulus under photocrosslinking by supplementing Ru/SPS and thermal crosslinking at physiological temperature (37 °C). All of the dERS concentration ranges (0.5, 1.5, and 3%) exhibited efficient photocrosslinking when visible light was used to irradiate the samples (Fig. 3F). Because the suitable storage modulus range of hydrogel for bioprinting is  $10^2$ – $10^3$  Pa<sup>34</sup> and the cell viability in viscous bioinks over 3% can decrease due to high shear stress,<sup>18</sup> 1.5% was chosen for SIS dECM subsequently (Fig. S1†).

## 3.2. Preparation of SIS GeldECM

**3.2.1. Development of SIS GeldECM.** The rich collagen components in the dECMs were denatured into gelatin through heat exposure (Fig. 4A). We hypothesized that the concentration of dECM and its gelatinization time would be critical parameters in a single hydrogel system. To mitigate the complexity introduced by an excessive combination of variables, we initially standardized the gelatinization time and began by exploring the crosslinking features of SIS dECM and GeldECM with a focus on varying concentration conditions. We evaluated the crosslinking properties of GeldECM treated for 3 h with thermal denaturation and determined the point at which dECM first becomes transparent due to gelatinization (Fig. 4B).

**3.2.2. Characterization of GeldECM.** We assessed the rheological properties of GeldECM and GeldERS at different concentrations. The change in the modulus of the GeldECM, while decreasing temperature from 37 °C to 4 °C, showed opposite thermodynamics compared to dECM (Fig. 4C). In terms of the proper storage modulus for bioprinting and cell viability, the candidate value was narrowed to 3% (Fig. S1†). In addition, the 3% group alone showed an instant increase in the complex modulus due to the photocrosslinking among the GeldERS (Fig. 4D). To separate the effects of photocrosslinking and physical entanglement, the GeldERS samples were analyzed at 37 °C. Because the GeldECM can only be permanently solidified through photocrosslinking, the 3% SIS GeldECM was chosen for the next steps.

## 3.2.3. Comprehensive study of the gelatinization time

**3.2.3.1. Mechanical properties.** We identified the characteristics of GeldECM according to the gelatinization time. Because the GeldECM serves as a rheological modifier of dECM, it is important to identify the alterations in its mechan-



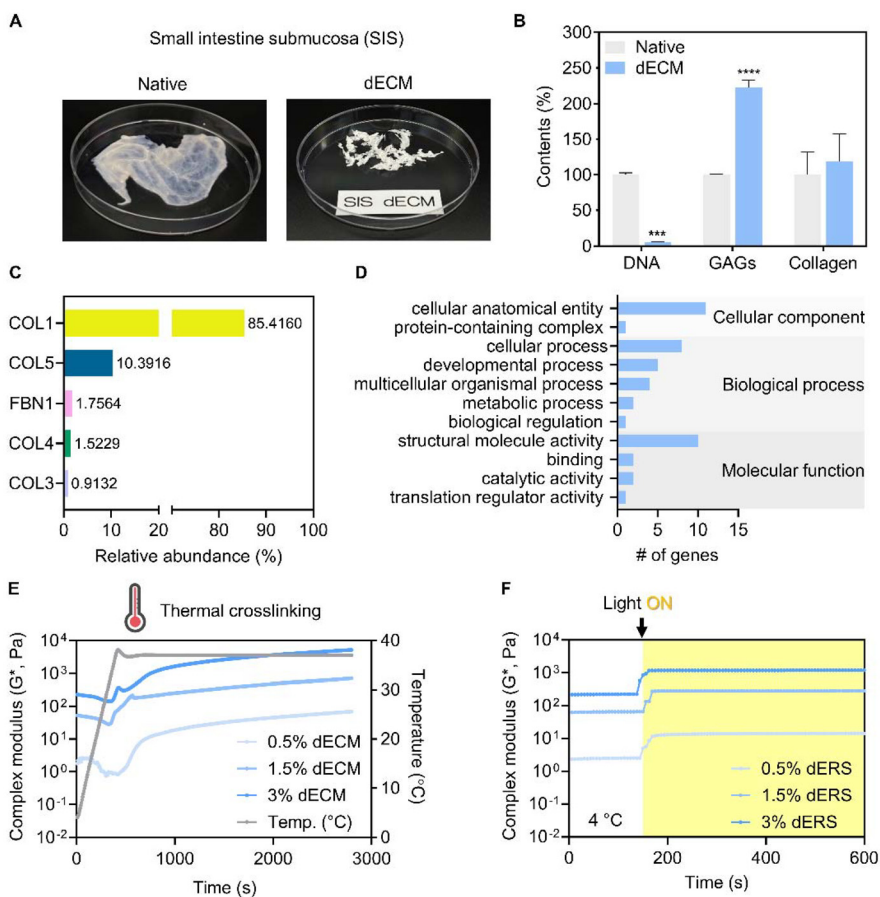


**Fig. 3** Development and characterization of SIS dECM. (A) Image of SIS native tissue and its decellularized sponge form. (B) Biochemical assays of native and decellularized SIS tissue; quantification of DNA, GAGs, and collagen contents. (C and D) Proteomic analysis of SIS dECM. (C) Relative abundance of the top 5 proteins in SIS dECM. (D) Gene ontology analysis of the SIS dECM. (E and F) Rheological analysis of SIS dECM at various concentrations. (E) Thermal crosslinking effect in SIS dECM measured by temperature ramp from 4 to 37 °C. (F) Photocrosslinking effect in SIS dERS measured by time sweep at 4 °C. Visible light irradiation started at 180 s. The biochemical assays and rheological analysis were conducted in triplicate. Bars:  $\pm$ S.D. (\*\*\*,  $p < 0.001$ ; \*\*\*\*,  $p < 0.0001$ ; otherwise not significant).

ical properties and adapt them as needed. For mechanical testing, GeldECMs with different gelatinization times (0, 3, 12, 24, 72, and 120 h) were supplemented with Ru/SPS and cast into molds to fabricate uniform specimens for compressive and tensile tests. However, samples from 72 and 120 h were excluded because they were not photocrosslinkable.

The compressive and tensile tests showed that gelatinization imparted ductile, stretchable, and tough nature on the stiff and brittle dECM (Fig. 5). Compression testing revealed a decrease in the compressive modulus and yield strength with gelatinization (Fig. 5A–C). The decrease in the compressive modulus indicates that GeldECM became more deformable and less stiff when subjected to compressive forces compared with dECM (Fig. 5B). For a given tensile force, the GeldECM showed higher ductility and stretchability (Fig. 5D–G). The decrease in tensile modulus indicates that the GeldECM became less stiff and experienced more significant elongation (Fig. 5E). Especially, the failure strain of SIS GeldECM increased significantly to approximately 120–130% compared with dECM, which is similar to the failure strain value of

native tissue of human small intestine, *i.e.*, 140% (Fig. 5F).<sup>35</sup> The toughness increased more than 2-fold after gelatinization (Fig. 5G).

This transformation indicates that GeldECM is soft yet tough, which is largely attributed to physical entanglements in the GeldECM hydrogel network. The physical entanglements function as flexible crosslinking points whereas the chemical crosslinking gives rigidity to the hydrogel.<sup>26</sup> Thus, balanced physical and chemical crosslinking in the network could have allowed the energy to dissipate efficiently.<sup>36</sup>

**3.2.3.2. Collagen integrity.** To reveal the mode of action of gelatinization, we traced the gelatinization-induced changes at the molecular level. Succeeding, we moved on to optimize the gelatinization time for our study. We analyzed the FTIR spectra of the SIS GeldECM by focusing on specific absorbance bands related to collagen structure, such as amides A, I, II, and III (Table 2). FTIR spectroscopy has been employed for the comprehensive examination of protein characteristics, including their secondary structure composition, structural dynamics, and conformational alterations triggered by variations in temp-





**Fig. 4** Development and characterization of SIS GeldECM. (A) Denaturation of dECM collagens to gelatin. (B) Change in transmittance induced by gelatinization of SIS dECM. (C and D) Rheological analysis of SIS GeldECM with different concentrations. (C) Thermal crosslinking effect in SIS GeldECM measured by temperature ramp from 37 to 4  $^{\circ}\text{C}$ . (D) Photocrosslinking effect in SIS GeldERS at 37  $^{\circ}\text{C}$ . Visible light irradiation started at 180 s. All experiments were performed in triplicate.



**Fig. 5** Compressive and tensile test of SIS GeldECMs according to gelatinization time. (A–C) Compressive test. (A) Compressive stress–strain curves, (B) compressive modulus, and (C) compressive yield strength. (D–G) Tensile test. (D) Tensile stress–strain curves, (E) tensile modulus, (F) elongation and break, and (G) toughness. All experiments were performed in triplicate. Bars:  $\pm$ S.D. (\*,  $p < 0.05$ ; \*\*\*,  $p < 0.001$ ; \*\*\*\*,  $p < 0.0001$ ; otherwise not significant).



**Table 2** FTIR spectra related to the integrity of collagen structure and denaturation

Designation	Approximate frequency (cm <sup>-1</sup> )	Description	Ref.
Amide A	3300–3500	Intermolecular hydrogen bonds Collagen triple helix structure	38, 40 and 41
Amide I	1600–1700	Secondary structural composition of the peptide Intramolecular hydrogen bonds	38 and 42
Amide II	1480–1575	Intact triple helical structure of collagens	38 and 42
Amide III	1200–1300	Formation of hydrogen bonds Collagen triple helix structure	39 and 40
AIII/A1450	1.00 for pure collagen 0.59 for denatured collagen	Hydrogen bonding of the collagen peptide bond Integrity of collagen triple helical structure	38
$\Delta\nu$ ( $\nu_{AI}-\nu_{AII}$ )	<100 cm <sup>-1</sup>	Denaturation of the secondary structure of collagen	43

**Table 3** Summary of changes in FTIR spectra attributed to gelatinization

Gelatinization time	Parameters					
	Amide A	Amide I	Amide II	Amide III	AIII/A1450	$\Delta\nu$
0 h	3411.923	1637.492	1546.842	1228.601	1.280	90.650
3 h	3400.351	1637.492	1546.842	1234.384	0.997	90.650
12 h	3408.066	1637.492	1546.842	1235.316	0.716	90.650
24 h	3411.923	1637.492	1546.842	1242.102	0.640	90.650
72 h	3409.995	1635.563	1544.913	1240.173	0.683	90.650
120 h	3408.066	1637.492	1546.842	1240.173	0.745	90.650

erature, pH, and pressure. We identified a red shift in the amide A band peak positions after heat exposure indicating that the structural order of collagen changed due to the disruption of hydrogen bonds (Table 3 and Fig. S2†).<sup>37–39</sup> Additionally, a blue shifting in the amide III frequency was observed, which is a typical response to the interruption in the hydrogen bonding of collagen.<sup>39</sup> These shifts in both amide A and amide III implied that the hydrogen bonding in collagen was disturbed leading to alteration in its structure during gelatinization.

Calculation of the intensity ratio of amide III to 1450 cm<sup>-1</sup> (AIII/A1450) and the wavenumber difference between amide I and II ( $\Delta\nu$ ) revealed detailed information about where the gelatinization-induced change happened among the three hierarchical levels of collagen's structure (Table 3). The AIII/A1450 ratio of SIS dECM was 1.280, which was similar to that of pure and intact collagen.<sup>38</sup> The gelatinization reduced the AIII/A1450 value to 0.997, suggesting a loss of triple helicity of collagen structure.<sup>44,45</sup> Meanwhile, the  $\Delta\nu$  value was consistently under 100 cm<sup>-1</sup>, disclosing that the secondary structure of the collagen did not denature during gelatinization.<sup>43</sup>

**3.2.3.3. Tyrosine moiety.** We confirmed that the tyrosine was abundant in dECM and did not notably decline, which assures efficient photocrosslinking of both dECM and GeldECM as tyrosine is the moiety necessary for photocrosslinking *via* Ru/SPS (Table 4 and Fig. S3†).

### 3.3. Comparison between dECM and GeldECM

To use GeldECM as a tissue-specific modifier, it is rational to clarify that gelatinization does not damage the bioactivity

**Table 4** The concentration of protein-bound tyrosine in SIS dECM and GeldECM

Gelatinization time	Concentration of tyrosine ( $\mu\text{g mL}^{-1}$ )
0 h	136.871
3 h	143.473
12 h	124.544
72 h	124.148
120 h	90.428

of dECM. GeldECM should hold tissue-specific micro-environmental cues to support cells and moieties for photocrosslinking. We analyzed and compared the ECM profiles of SIS dECM and 3 h heat-treated GeldECM. The number of proteins that were classified as matrisomes was determined among all proteins identified (Fig. 6A). SIS dECM and GeldECM had a similar ratio of matrisome proteins in their components. We compared the top 5 proteins and collagen types in the SIS dECM and GeldECM. SIS GeldECM presented a significant similarity in the composition of their top 5 proteins and collagens compared with SIS dECM (Fig. S4† and Fig. 6B). They shared three collagen types, I, III, and VI, showing compositional similarity. The SIS dECM and SIS GeldECM have four collagen types in common, indicating that gelatinization did not alter their collagen constitution.<sup>35</sup>

To verify the change in molecular weight, we conducted SDS-PAGE (Fig. 6C and Fig. S5†). Because there were no considerable alternations in their band location and width, the proteins were denatured minimally and the triple helix of col-







**Fig. 6** Comparison between dECM and GeldECM. (A–C) Compatible bioactivity of GeldECM. (A) The percentage of matrisome proteins out of total proteins and (B) the top 5 abundant collagen types in SIS dECM and GeldECM. (C) Change in molecular weight induced by gelatinization. (D–G) Instantaneous enhancement of rheological properties induced by gelatinization. (D) Viscosity profile over shear rates ranging from  $10^0$  to  $10^2$   $s^{-1}$  and (E) at  $10^1$   $s^{-1}$ . (F and G) Complex modulus under a 2% strain. (G) The bar graph was generated at 600 s. Rheological analyses were performed in triplicate. Bars:  $\pm$ S.D. (\*\*,  $p < 0.01$ ; \*\*\*,  $p < 0.001$ ).

lagen unraveled partially after gelatinization. It has been reported that no changes in the position or thickness of the bands were detected on the SDS-PAGE in the case of partial unraveling.<sup>46</sup> The dECM and GeldECM showed negligible dispersion of bands in the molecular weight range of the collagen helix, approximately 300 kDa,<sup>47</sup> confirming that the partial disentangling of collagen was induced by gelatinization. Overall, regulating the temperature within a range encompassing both collagen denaturation and heat inactivation ensures the preservation of key biological factors of dECM hydrogels.<sup>32</sup>

Rheological characterization showed instantly enhanced viscosity and modulus in GeldECM (Fig. 6D–G). Gelatinization significantly increased the viscosity and modulus of dECM more than 2-fold (Fig. 6E) and 1.7-fold effortlessly due to the spontaneous physical entanglement at printing temperature (4 °C) (Fig. 6G).

### 3.4. Rheological properties of hybrid ratio

Because the SIS GeldECM displayed considerably different mechanical properties compared with the SIS dECM, we blended GeldECM with dECM to modulate the rheological properties of the resultant hybrid bioink and the mechanical properties of the printed constructs. We screened various hybrid ratios between SIS dECM and GeldECM to achieve the ultimate mechanical properties through the triple crosslinking strategy.

First, we evaluated the suitability of the hybrid bioinks for extrusion-based printing with various blending ratios, 10:0, 9:1, 7:3, and 5:5, (dECM to GeldECM) at different tempera-

tures (Fig. S6†). The viscosity profiles exhibited shear-thinning properties implying that they can be used for extrusion-based printing. We then evaluated the effect of sequential double crosslinking in the hybrid bioinks (Fig. 7A and B). The hybrid bioinks containing more than 30% GeldECM (d7G3 and d5G5) displayed significantly higher modulus compared with dECM (d10G0) because of the high packing density of GeldECM through physical crosslinking (Fig. 7B).

Furthermore, we investigated the impact of successive additions of the thermal crosslinking step (Fig. 7C and D). It was found that the triple crosslinking of bioinks greatly increased the modulus at least 3-fold to a maximum of 32-fold compared to double crosslinking (Fig. 7D). Notably, during the early stages of thermal crosslinking (500 to 1000 s), the modulus of bioinks fluctuates (Fig. 7C). This is because of the thermodynamics during the crosslinking of collagen; the triple helical structure of collagen is partially unwound as the increased temperature gives kinetic energy to overcome the hydrogen bonds maintaining it.<sup>48</sup> Subsequently, during the later stages of crosslinking, the collagen molecules reassemble and form covalent bonds, creating a more stabilized and cross-linked structure.

Among the aforementioned three candidate groups (d7G3 and d5G5), the d7G3 hybrid group showed similar depth and span of fluctuations to dECM (d10G0), while having a significantly higher modulus when the crosslinking was complete. Meanwhile, the 5:5 hybrid group presented a huge decrease in modulus during thermal crosslinking, which resulted in



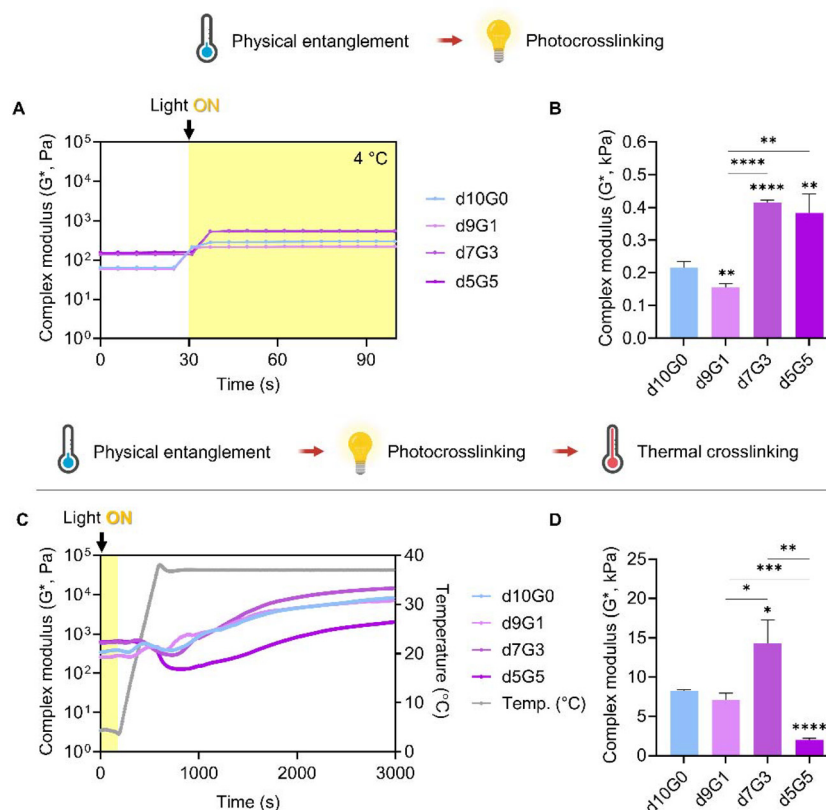


**Fig. 7** Rheological analysis of the multiple crosslinking strategies using hybrid bioinks. (A and B) The effect of sequential double crosslinking consists of physical entanglement and photocrosslinking. (A) Time sweep of the hybrid bioinks. Visible light irradiation starts at 30 s. (B) Complex modulus of the hybrid bioinks after dual crosslinking. (C and D) Effect of sequential triple crosslinking. (C) Temperature ramp of the hybrid bioinks. The visible light was irradiated for 3 min. (D) Complex modulus of the hybrid bioinks after triple crosslinking. All experiments were performed in triplicate. Bars:  $\pm$ S.D. (\*,  $p < 0.05$ ; \*\*,  $p < 0.01$ ; \*\*\*,  $p < 0.001$ ; \*\*\*\*,  $p < 0.0001$ ; otherwise not significant).

lower stiffness than the dECM group. Crosslinking was hindered at this specific ratio; although each component of the composite hydrogel is stable and crosslinkable, at some ratio they may disrupt the intermolecular crosslinking reaction with

one another.<sup>49,50</sup> Based on these results, we proceeded to print with the d7G3 hybrid bioink compared with dECM. We named this optimized hybrid condition a mechanically tuned tissue-specific bioink (MeTTi-dECM).

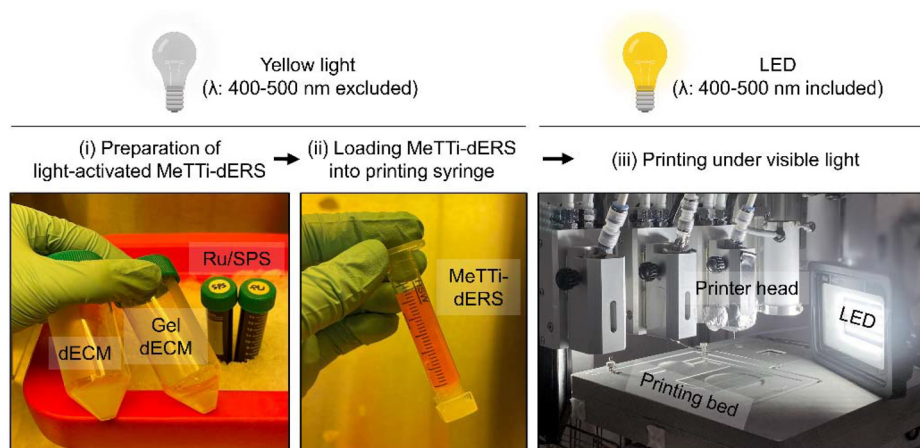


**Fig. 8** Preparation of MeTTi-dERS and the printing set-up.



### 3.5. Printability assessment of the MeTTi-dERS

Next, we evaluated whether the MeTTi-dECM can enhance the printability of the dECM. We established a printing environment that does not activate the photocrosslinking of dERS or

MeTTi-dERS during bioink preparation, but instantly activates photocrosslinking during printing by adjusting illumination (Fig. 8).

Extrusion-based printing offers an appealing feature in its ability to freely draw intricate details with high resolution

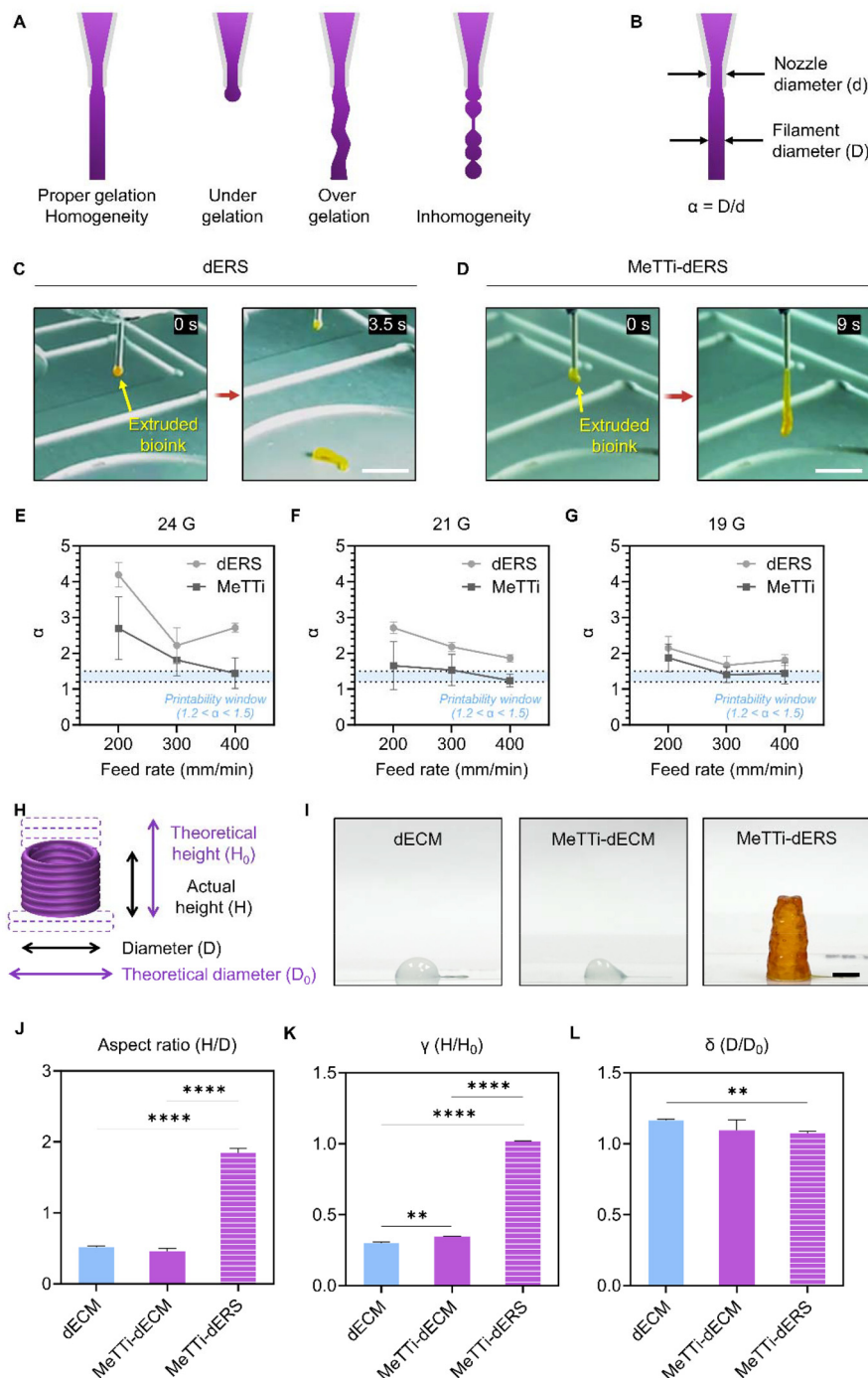


**Fig. 9** Printability assessment of MeTTi-dERS. Schematic of (A) strand formation test and (B)  $\alpha$  value. (C and D) The strands were extruded at the same condition; 19 G, 5 kPa. Scale bar: 1 cm. (E–G) The  $\alpha$  value distribution at the same condition; 20 kPa for 24 G, 10 kPa for 21 G, and 7.5 kPa for 19 G were used. (H) Schematic of aspect ratio,  $\gamma$ , and  $\delta$  values. (I) Images of tissues with the same stacked layers. Scale bar: 0.5 cm. Quantification of (J) aspect ratio, (K)  $\gamma$ , and (L)  $\delta$  values of the printed tissues from (I). All experiments were performed in triplicate. Bars:  $\pm$ S.D. (\*\*,  $p < 0.01$ ; \*\*\*\*,  $p < 0.0001$ ; otherwise not significant).



using finely extruded ink lines. The increased adjustability of the width of the printed line directly correlates with the enhanced shape fidelity of the intended structure.<sup>14</sup> To demonstrate line adjustability, we printed dERS and MeTTi-dERS under various conditions, while manipulating parameters, such as nozzle size, pneumatic pressure during dispensing, and motion speed of the printer head (feed rate; abbreviated as F) (Fig. 9A–G). We chose 24, 21, and 19 gauges (abbreviated as G) as representatives for thin, moderate, and thick nozzles, respectively.

The strand formation test assesses static extrusion pressure, ink gelation status, and strand uniformity, providing a brief insight into the hydrogel's 3D printing capabilities (Fig. 9A).<sup>51</sup> Because the MeTTi-dERS is a composite hydrogel consisting of two different gels with opposite thermodynamic behavior, it may cause inhomogeneity in the ink, hindering the formation of straight strands. We extruded the two bioinks through the 19 G nozzle at 5 kPa for the longest time until the strands were removed (Fig. 9C and D). With the strand formation test, we confirmed the homogeneity of the bioinks from their uniform strands. Remarkably, the MeTTi-dERS produced a much longer strand compared with dECM, indicating that the MeTTi-dERS is more strongly gelatinized to withstand the weight of the strand.

When the ink is extruded out of the nozzle, it expands because of the release of shear stress, increasing the filament diameter. Previously, an  $\alpha$  value, *i.e.*, the ratio between the filament diameter and the nozzle diameter (Fig. 9B), was introduced to describe the spread of the printed filament.<sup>33</sup> Quantifying the  $\alpha$  values from the line structures printed using dECM and MeTTi-dERS reveals that more  $\alpha$  values fell within the printable range,  $1.2 < \alpha < 1.5$ , in the MeTTi-dERS group under the same printing conditions (Fig. 9E–G).

To address the imperative need in regenerative medicine for fabricating elongated tissues that are commensurate with the size of defects, we evaluated the aspect ratio,  $\gamma$ , and  $\delta$  values (Fig. 9H–L, ESI movies 1 and 2†). The aspect ratio is expressed as  $H/D$ , where  $H$  is the actual height and  $D$  is the diameter of the stacked constructs (Fig. 9H and I). Quantification of aspect ratios revealed significantly increased stacked height when using MeTTi-dERS, underscoring the effectiveness of the sequentially added-up triple crosslinking strategy (Fig. 9J). The  $\gamma$  value, which describes the sinking degree of the stacked constructs and is denoted as  $H/H_0$ , is the ratio between the actual and theoretical heights (Fig. 9H). The MeTTi-dERS showed a significantly higher  $\gamma$  value compared with the other groups, indicating that it accurately matches the initially designed dimensions (Fig. 9K). Lastly, stacking the hydrogel structure often encounters the problem of filament diffusion in the bottom layers. This degree of diffusion can be expressed as  $\delta$ , which is the ratio of the actual and theoretical diameters (Fig. 9H). The MeTTi-dECM had a smaller  $\delta$  value, indicating less horizontal diffusion of the printed filaments when stacked (Fig. 9L).

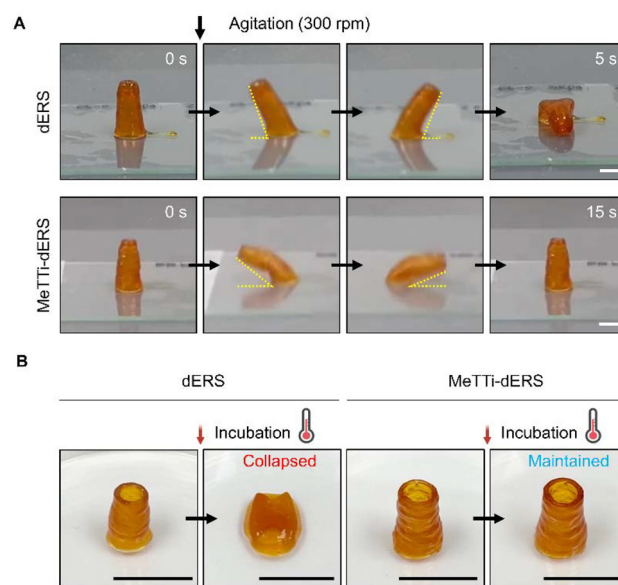


**Fig. 10** Structural integrity assessment of the printed tissues. (A) Evaluation of tissue resilience using an orbital rocker. Scale bar: 1 cm. (B) Stability of the printed constructs during incubation at 37 °C for 40 min. Scale bar: 1 cm.

### 3.6. Structural integrity assessment of printed tissues

Tissue resilience was remarkably different across the samples (Fig. 10A, ESI movies 3 and 4†). We agitated the dERS and MeTTi-dERS tissues with the same aspect ratio on an orbital shaker at 300 rpm before thermal crosslinking. The dERS collapsed 5 s after agitation, whereas the MeTTi-dERS withstood agitation for 15 s and recovered to its original shape. This clearly shows their capability to dissipate energy through flexible physical crosslinking points within the hydrogel network. In addition, thermal crosslinking made the dERS tissue unstable, as previously predicted by rheology data, which obstructs the steady culture of tissues with a high aspect ratio or structural complexity (Fig. 10B). Notably, the MeTTi-dERS tissues maintained their shape during incubation, which is possibly attributed to the high modulus obtained from triple crosslinking. Prolonged culture dissolved the unreacted Ru/SPS in the printed tissues without disturbing tissue integrity (Fig. S8†).

### 3.7. Biological assessment of printed tissues

As observed in the rheological analysis, bioinks have high viscosity. Therefore, it is essential to establish the conditions suitable for high printability and cellular assessments. Before the fabrication of tissues, we checked the viability of cells printed with the bioinks using Caco-2 cells (Fig. 11A and B). Using a 19 G nozzle, both dERS and MeTTi-dERS demonstrated a high viability of more than 80%, and there was no significant difference between the groups (Fig. 11C). They also showed good





**Fig. 11** Biological assessment of dERS and MeTTi-dERS. (A and B) Images of live/dead tissue and (C–E) their cell viability quantification. Scale bar: 500  $\mu$ m. (F–H) Evaluation of tissue maturation. (F) Illustration of the area where IF imaging was performed. (G) Mucin expression and (H) E-CAD expression at day 7 in the dERS and MeTTi-dERS tissues. Scale bar: 1000 and 200  $\mu$ m, respectively. All experiments were performed in triplicate. Bars:  $\pm$ S.D. (ns, not significant).

viability of over 70% in the 21 G and 24 G conditions (Fig. 11D and E).

Lastly, we evaluated the maturation of printed tissues (Fig. 11F–H). IF staining of mucin revealed that the dERS and MeTTi-dERS tissues exhibited comparable levels of mucin expression (Fig. 11G). Furthermore, we evaluated the expression of junctional protein markers, E-CAD, in the tissues as Caco-2 is an enterocyte that is responsible for forming the intestinal epithelium (Fig. 11H). We observed comparable expression of this junctional protein and a barrier-like morphology in both groups. Overall, intestinal tissues bioprinted with MeTTi-dERS denoted excellent printability, structural integrity, and biological function.

## 4. Conclusions

In summary, we used GelDECM as a rheological modifier and developed MeTTi-dERS, which has superior mechanical properties because of its inherent physical entanglement. To the best of our knowledge, this is the first report on a tissue-specific rheological modifier. The tissues printed with MeTTi-dERS showed improved printability, shape fidelity, and structural integrity compared with other bioinks based on dECM with single or double crosslinking sequences and excellent biological function. Taken together, the proposed strategy employing GelDECM as a rheology modifier of dECM opens new avenues for fabricating soft and flexible *in vitro* tissues.



## Author contributions

Hohyeon Han, Minji Kim: conceptualization, methodology, validation, formal analysis, investigation, writing – original draft, writing – review & editing, and visualization. Uijung Yong: methodology, validation, formal analysis, and investigation. Yeonggwon Jo: validation and investigation. Yoo-mi Choi, Hye Jin Kim, and Dong Gyu Hwang: investigation. Dayoon Kang: investigation and resources. Jinah Jang: conceptualization, methodology, writing – review & editing, supervision, project administration, and funding acquisition.

## Conflicts of interest

There are no conflicts to declare.

## Acknowledgements

This work was supported by the National Research Foundation of Korea (NRF) grant funded by the Korean government (MSIT) (No. 2021R1A2C2004981). This work was also supported by the Alchemist Project 1415180884 (20012378, Development of Meta Soft Organ Module Manufacturing Technology without Immunity Rejection and Module Assembly Robot System) and the Technology Development Program (S3318933) funded by the Ministry of Trade, Industry & Energy (MOTIE) and the Ministry of SMEs and Startups (MSS) in Korea, respectively.

## References

- B. S. Kim, S. Das, J. Jang and D.-W. Cho, *Chem. Rev.*, 2020, **120**, 10608–10661.
- W. Han, N. K. Singh, J. J. Kim, H. Kim, B. S. Kim, J. Y. Park, J. Jang and D. W. Cho, *Biomaterials*, 2019, **224**, 119496.
- D. O. Freytes, J. Martin, S. S. Velankar, A. S. Lee and S. F. Badylak, *Biomaterials*, 2008, **29**, 1630–1637.
- J. Yoon and J. Jang, Decellularized Tissue-Derived Materials as Advanced Bioinks, in *Handbook of the Extracellular Matrix*, ed. F. R. A. Maia, J. M. Oliveira and R. L. Reis, Springer International Publishing, Cham, 2023, pp. 1–43.
- A. A. Golebiowska, J. T. Intravaia, V. M. Sathe, S. G. Kumbar and S. P. Nukavarapu, *Bioact. Mater.*, 2024, **32**, 98–123.
- M. T. Spang and K. L. Christman, *Acta Biomater.*, 2018, **68**, 1–14.
- J. H. Traverse, T. D. Henry, N. Dib, A. N. Patel, C. Pepine, G. L. Schaer, J. A. DeQuach, A. M. Kinsey, P. Chamberlin and K. L. Christman, *JACC: Basic Transl. Sci.*, 2019, **4**, 659–669.
- J. A. Serna, L. Rueda-gensini, D. N. Céspedes-valenzuela, J. Cifuentes, J. C. Cruz and C. Muñoz-camargo, *Polymers*, 2021, **13**, 3263.
- Z. Galliger, C. D. Vogt and A. Panoskaltis-Mortari, *Transl. Res.*, 2019, **211**, 19–34.
- H. Nam, H. J. Jeong, Y. Jo, J. Y. Lee, D. H. Ha, J. H. Kim, J. H. Chung, Y. S. Cho, D. W. Cho, S. J. Lee and J. Jang, *Sci. Rep.*, 2020, **10**, 1–14.
- K. Esmaeili Pourfarhangi, S. Mashayekhan, S. G. Asl and Z. Hajebrahimi, *Biologicals*, 2018, **53**, 10–18.
- B. Nyambat, Y. B. Manga, C.-H. Chen, U. Gankhuyag, A. Pratomo WP, M. Kumar Satapathy and E.-Y. Chuang, *Int. J. Mol. Sci.*, 2020, **21**, 4864.
- Y. E. Arslan, Y. F. Galata, T. Sezgin Arslan and B. Derkus, *J. Mater. Sci. Mater. Med.*, 2018, **29**, 127.
- J. Jang, T. G. Kim, B. S. Kim, S. W. Kim, S. M. Kwon and D. W. Cho, *Acta Biomater.*, 2016, **33**, 88–95.
- G. Gao, H. Kim, B. S. Kim, J. S. Kong, J. Y. Lee, B. W. Park, S. Chae, J. Kim, K. Ban, J. Jang, H. J. Park and D. W. Cho, *Appl. Phys. Rev.*, 2019, **6**, 041402.
- X. Ma, C. Yu, P. Wang, W. Xu, X. Wan, C. S. E. Lai, J. Liu, A. Koroleva-Maharajh and S. Chen, *Biomaterials*, 2018, **185**, 310–321.
- J. Yoon, H. Han and J. Jang, *Nano Convergence*, 2023, **10**, 52.
- J. Lee, J. Hong, W. J. Kim and G. H. Kim, *Carbohydr. Polym.*, 2020, **250**, 116914.
- D. O. Visscher, H. Lee, P. P. M. van Zuijlen, M. N. Helder, A. Atala, J. J. Yoo and S. J. Lee, *Acta Biomater.*, 2021, **121**, 193–203.
- M. Ali, A. K. PR, J. J. Yoo, F. Zahran, A. Atala and S. J. Lee, *Adv. Healthc. Mater.*, 2019, **8**, 1800992.
- H. Kim, B. Kang, X. Cui, S. H. Lee, K. Lee, D. W. Cho, W. Hwang, T. B. F. Woodfield, K. S. Lim and J. Jang, *Adv. Funct. Mater.*, 2021, **31**, 2011252.
- H. Zhang, Y. Wang, Z. Zheng, X. Wei, L. Chen, Y. Wu, W. Huang and L. Yang, *Theranostics*, 2023, **13**, 2562–2587.
- C. K. Kuo and P. X. Ma, *J. Biomed. Mater. Res., Part A*, 2008, **84**, 899–907.
- D. C. Bassett, A. G. Hâti, T. B. Melø, B. T. Stokke and P. Sikorski, *J. Mater. Chem. B*, 2016, **4**, 6175–6182.
- Y. J. Shin, R. T. Shafraneck, J. H. Tsui, J. Walcott, A. Nelson and D. H. Kim, *Acta Biomater.*, 2021, **119**, 75–88.
- M. Wang, S. Sun, G. Dong, F. Long and J. T. Butcher, *Proc. Natl. Acad. Sci. U. S. A.*, 2023, **120**, e2213030120.
- G. Su, Y. Zhang, X. Zhang, J. Feng, J. Cao, X. Zhang and T. Zhou, *Chem. Mater.*, 2022, **34**, 1392–1402.
- H. Kim, B. Kang, X. Cui, S. H. Lee, K. Lee, D. W. Cho, W. Hwang, T. B. F. Woodfield, K. S. Lim and J. Jang, *Adv. Funct. Mater.*, 2021, **31**, 2011252.
- H. Han, Y. Park, Y. mi Choi, U. Yong, B. Kang, W. Shin, S. Min, H. J. Kim and J. Jang, *Adv. Healthc. Mater.*, 2022, **11**, 2101768.
- F. Pati, J. Jang, D. H. Ha, S. Won Kim, J. W. Rhie, J. H. Shim, D. H. Kim and D. W. Cho, *Nat. Commun.*, 2014, **5**, 3935.
- K. S. Lim, R. Levato, P. F. Costa, M. D. Castilho, C. R. Alcalá-Orozco, K. M. A. Van Dorenmalen, F. P. W. Melchels, D. Gawlitta, G. J. Hooper, J. Malda and T. B. F. Woodfield, *Biofabrication*, 2018, **10**, 034101.



- 32 H. Kim, J. H. Jang, W. Han, H. J. Hwang, J. Jang, J. Y. Kim and D. W. Cho, *Biomaterials*, 2023, **292**, 121941.
- 33 Q. Gao, X. Niu, L. Shao, L. Zhou, Z. Lin, A. Sun, J. Fu, Z. Chen, J. Hu, Y. Liu and Y. He, *Biofabrication*, 2019, **11**, 035006.
- 34 N. Ashammakhi, S. Ahadian, C. Xu, H. Montazerian, H. Ko, R. Nasiri, N. Barros and A. Khademhosseini, *Mater. Today Bio*, 2019, **1**, 100008.
- 35 V. I. Egorov, I. V. Schastlivtsev, E. V. Prut, A. O. Baranov and R. A. Turusov, *Mechanical properties of the human gastrointestinal tract*, 2002, vol. 35.
- 36 C. Norioka, Y. Inamoto, C. Hajime, A. Kawamura and T. Miyata, *NPG Asia Mater.*, 2021, **13**, 34.
- 37 O. S. Rabotyagova, P. Cebe and D. L. Kaplan, *Mater. Sci. Eng., C*, 2008, **28**, 1420–1429.
- 38 T. Riaz, R. Zeeshan, F. Zarif, K. Ilyas, N. Muhammad, S. Z. Safi, A. Rahim, S. A. A. Rizvi and I. U. Rehman, *Appl. Spectrosc. Rev.*, 2018, **53**, 703–746.
- 39 N. S. Myshakina, Z. Ahmed and S. A. Asher, *J. Phys. Chem. B*, 2008, **112**, 11873–11877.
- 40 J. H. Muyonga, C. G. B. Cole and K. G. Duodu, *Food Chem.*, 2004, **86**, 325–332.
- 41 Y. Ji, X. Yang, Z. Ji, L. Zhu, N. Ma, D. Chen, X. Jia, J. Tang and Y. Cao, *ACS Omega*, 2020, **5**, 8572–8578.
- 42 J. Kong and S. Yu, *Acta Biochim. Biophys. Sin.*, 2007, **39**, 549–559.
- 43 M. G. Albu, M. V. Ghica, M. Giurginca, V. Trandafir, L. Popa and C. Cotrut, *Rev. Chim.*, 2009, **60**, 666–672.
- 44 B. F. D. Zaelani, M. Safithri, K. Tarman, I. Setyaningsih and M. Meydia, *IOP Conf Ser Earth Environ Sci*, DOI: [10.1088/1755-1315/241/1/012033](https://doi.org/10.1088/1755-1315/241/1/012033).
- 45 A. Pielesz, *Spectrochim. Acta, Part A*, 2014, **118**, 287–293.
- 46 M. Sun, X. Wei, H. Wang, C. Xu, B. Wei, J. Zhang, L. He, Y. Xu and S. Li, *Food Bioprocess Technol.*, 2020, **13**, 367–378.
- 47 A. León-López, A. Morales-Peñalosa, V. M. Martínez-Juárez, A. Vargas-Torres, D. I. Zeugolis and G. Aguirre-Álvarez, *Molecules*, 2019, **24**, 4031.
- 48 T. L. Willett, R. S. Labow, N. C. Avery and J. M. Lee, *Ann. Biomed. Eng.*, 2007, **35**, 1961–1972.
- 49 J. E. Torres, F. Meng, S. Bhattacharya, K. P. Buno, A. Ahmadzadegan, S. Madduri, P. M. Babiak, P. P. Vlachos, L. Solorio, Y. Yeo and J. C. Liu, *Biomacromolecules*, 2023, **24**, 4718–4730.
- 50 Y. He, Z. Hou, J. Wang, Z. Wang, X. Li, J. Liu, X. Yang, Q. Liang and J. Zhao, *Int. J. Biol. Macromol.*, 2020, **149**, 1275–1284.
- 51 F. F. Cai, S. Heid and A. R. Boccaccini, *J. Biomed. Mater. Res., Part B*, 2021, **109**, 1090–1104.

